HHS Public Access

Author manuscript

Neuroimage. Author manuscript; available in PMC 2024 July 22.

Published in final edited form as:

Neuroimage. 2022 August 01; 256: 119216. doi:10.1016/j.neuroimage.2022.119216.

Open-source FlexNIRS: A low-cost, wireless and wearable cerebral health tracker

Kuan-Cheng Wu[a,b,*], **Davide Tamborini**[a], **Marco Renna**[a], **Adriano Peruch**[a], **Yujing Huang**[a], **Alyssa Martin**[a], **Kutlu Kaya**[a], **Zachary Starkweather**[a], **Alexander I. Zavriyev**[a], **Stefan A. Carp**[a], **David H. Salat**[a], **Maria Angela Franceschini**[a]

[a]Athinoula A. Martinos Center for Biomedical Imaging, Massachusetts General Hospital, 149 13th Street, Charlestown, MA 02129, USA

[b]Department of Biomedical Engineering, Boston University, 44 Cummington Mall, Boston, MA 02215, USA

Abstract

Currently, there is great interest in making neuroimaging widely accessible and thus expanding the sampling population for better understanding and preventing diseases. The use of wearable health devices has skyrocketed in recent years, allowing continuous assessment of physiological parameters in patients and research cohorts. While most health wearables monitor the heart, lungs and skeletal muscles, devices targeting the brain are currently lacking. To promote brain health in the general population, we developed a novel, low-cost wireless cerebral oximeter called FlexNIRS. The device has 4 LEDs and 3 photodiode detectors arranged in a symmetric geometry which allows for a self-calibrated multi-distance method to recover cerebral hemoglobin oxygenation (SO_2) at a rate of 100 Hz. The device is powered by a rechargeable battery and uses Bluetooth Low Energy (BLE) for wireless communication. We developed an Android application for portable data collection and real-time analysis and display. Characterization tests in phantoms and human participants show very low noise (noise-equivalent power <70 fW/ √Hz) and robustness

*Corresponding author at: Department of Biomedical Engineering, Boston University, 44 Cummington Mall, Boston, MA 02215, USA. kuan1031@bu.edu (K.-C. Wu).

Declaration of Competing Interest

DHS has a financial interest in Niji Corp, a company developing a suite of home/remote usage digital biomarker tools for the identification and assessment of individuals with Alzheimer's disease. MAF has a financial interest in 149 Medical, Inc., a company developing diffuse correlation spectroscopy technology for assessing and monitoring cerebral blood flow in newborn infants. DHS and MAF interests were reviewed and are managed by Massachusetts General Hospital and Mass General Brigham in accordance with their conflict of interest policies.

Credit authorship contribution statement

Kuan-Cheng Wu: Methodology, Software, Validation, Formal analysis, Investigation, Data curation, Writing – original draft, Writing – review & editing, Visualization. **Davide Tamborini:** Methodology, Resources. **Marco Renna:** Methodology, Validation, Resources, Investigation, Writing – original draft, Writing – review & editing, Visualization. **Adriano Peruch:** Methodology, Resources, Validation. **Yujing Huang:** Software. **Alyssa Martin:** Investigation. **Kutlu Kaya:** Investigation. **Zachary Starkweather:** Investigation. **Alexander I. Zavriyev:** Investigation. **Stefan A. Carp:** Conceptualization, Investigation, Resources, Supervision, Funding acquisition. **David H. Salat:** Conceptualization, Supervision, Funding acquisition. **Maria Angela Franceschini:** Conceptualization, Methodology, Resources, Writing – review & editing, Visualization, Supervision, Project administration, Funding acquisition.

Supplementary materials

Supplementary material associated with this article can be found, in the online version, at doi:10.1016/j.neuroimage.2022.119216.

of SO_2 quantification *in vivo*. The estimated cost is on the order of $50/unit for 1000 units, and our goal is to share the device with the research community following an open-source model. The low cost, ease-of-use, smart-phone readiness, accurate SO_2 quantification, real time data quality feedback, and long battery life make prolonged monitoring feasible in low resource settings, including typically medically underserved communities, and enable new community and telehealth applications.

Keywords

Cerebral oximetry; NIRS; Community health; Wearable device; Bluetooth low energy

1. Introduction

The use of wearable health devices has risen rapidly over the last several years (Seneviratne et al., 2017), with several wearable devices using light to monitor heart rate (HR) (Fuller et al., 2020), heart rate variability (HRV) (Georgiou et al., 2018), respiratory rate (Johnston and Mendelson, 2004; Pimentel et al., 2015; Singh et al., 2020) and pulse oximetry-derived peripheral capillary oxygen saturation (SpO_2) (Buekers et al., 2019; Huang et al., 2014; Kim et al., 2017). However, a wearable device that monitors cerebral oxygenation is missing from the market, despite the potential benefits of wearable neuromonitoring available to the general population.

Near-infrared spectroscopy (NIRS) is an established methodology which allows for the non-invasive monitoring of hemoglobin oxygen saturation (SO_2) in biological tissues. The technology has been adopted in the clinical space to detect cerebral hypoxia during surgery and in neuro intensive care settings (Green et al., 2016; Hogue et al., 2021). Several commercially available cerebral oximeters have received Food and Drug Administration (FDA) clearance (Benni et al., 2018; Pollard et al., 1996). These commercial devices comprise a control/display unit and a disposable sensor and are only suitable for bedside clinical applications. The limited wearability of these cerebral oximeters limits their use in the community health context.

Cerebral SO_2 monitoring at a community level and in tele-health applications may aid in the prevention or early detection of diseases like sleep apnea, stroke, and other cerebrovascular diseases. It could result in a significant reduction of subsequent medical costs and increased quality of life.

With the progress of optoelectronic technology, cerebral oximeters can now be miniaturized and made wearable. This has been shown by the many wearable functional near-infrared spectroscopy devices built in the last few years by both academic labs and industry producers (Pinti et al., 2018; Piper et al., 2014; von Lühmann et al., 2020). Functional NIRS devices are multichannel systems used to detect cerebral activity by measuring changes in oxy- and deoxy-hemoglobin concentrations. While in principle they can be modified to measure cerebral oxygenation, the multichannel electronics used are not well suited for oximetry applications for which a limited number of sources and detectors are sufficient,

but performance parameters are very stringent. In addition to the hardware performance, optimized device geometry and algorithms to extract a robust SO_2 signal are needed, as well as simple to use smartphone l compatible apps to collect and visualize data.

Recently, Rwei et al. (2020) developed a wearable cerebral oximeter for use solely in the pediatric population. This oximeter uses two source-detector separations (1.5 and 2.0 cm) for linear multi-distance cerebral oxygenation at a 100 Hz sampling rate with a low-pass cutoff frequency of 6.4 Hz. Due to the lower requirements for penetration depth in the pediatric demographic, the source-detector separations are shorter than standard cerebral oximetry devices. To achieve sufficient sensitivity for brain tissue in adults, longer source-detector separations are needed while still maintaining high sampling rate and good signal-to-noise ratio (SNR).

To fulfill these needs, we have developed a novel wireless and wearable cerebral oximeter and a corresponding mobile application for Android devices to promote health in the general population, with a focus on monitoring brain health in older adults, who are generally at risk for a range of brain diseases. The device is easy to use, insensitive to motion, and provides feedback to robustly measure SO_2 without the need of calibration. We have named this device FlexNIRS, given our use of flexible materials for both comfort and optimal measurement quality. Flexible components include the printed circuit board (PCB) of the optical probe and the casing material. We designed FlexNIRS to be very low cost to enable large-scale monitoring and research programs in low-resource settings. Ultimately, this device will provide personalized monitoring and cerebral health assessment that can be performed daily at home. FlexNIRS will facilitate the expansion of sampling size in neuroimaging studies for a better understanding. We are making this cerebral health tracker open source to reach underserved communities, including rural and low socioeconomic status populations.

2. Materials and methods

2.1. Instrument requirements

The key aspects for a personalized cerebral health tracker are:

- Low cost to allow consumer use and reach the wider underserved population;
- Easy to wear, lightweight and very low-profile;
- Wireless communication to enable complete freedom of movement and continuous wearing;
- Long battery life with rechargeable batteries;
- Motion compatibility;
- Reliable SO_2 readout values without the need for calibration;
- App-based interface to allow for remote monitoring and real-time feedback. This interface must also send an alert when detecting abnormalities, enabling timely intervention to prevent progression to a debilitating condition.

As detailed in the following sections, we aimed to fulfill all of these requirements in our design of the FlexNIRS.

2.2. Instrument design

The system concept of FlexNIRS is shown in the graphical abstract. The wearable wireless device consists of a 2-wavelength 6-channel continuous wave (CW) NIRS flex probe, an analog front-end (AFE) and digitization board, a Bluetooth Low Energy (BLE) control board and a rechargeable battery. To realize the concept, we developed a prototype including the hardware and the software for the device and a corresponding mobile app. In Fig. 1 we show a photograph of the wearable device, and in Fig. 2 we show the simplified schematic block diagram.

The flex probe hosts two dual color (735 nm and 850 nm) LED light sources and three photodiode detectors and is realized in a flexible printed circuit, which allows for adapting the probe to the surface of the forehead and guarantees good contact with the skin. The probe hosts both long (2.8 cm and 3.3 cm) and short (0.8 cm) source-detector separations.

The AFE and digitization board (see AFE Module in Figs. 1 and 2) hosts a specialized AFE chip designed for ECG (not implemented) and optical biosensing applications, such as heart-rate monitoring and peripheral capillary oxygen saturation. The AFE has a timing engine for creating customized acquisition sequences of source-detector pairs, a transmitter section for driving alternatively up to four LEDs light sources, and a receiver section for three photodiodes' inputs through a differential multiplexer. The photodiode signal is amplified and converted into a digital value by the embedded front-end and readout circuit. The high reconfigurability of the device allows us to adjust: the period of the on-time (temporal multiplexing), the driving current for each of the four LEDs, and the parameters for preliminary filtering, amplification, sampling, and digitization of each of the three photodetector signals.

The BLE control board (see BLE Module in Figs. 1 and 2) hosts a system-in-package (SiP) chip, an inertial module to detect movements, and power supply management circuitry. The SiP embeds a microcontroller (μC) and a BLE module with an integrated antenna for wireless data transmission. The Sip chip has a small form factor ($6.5 \times 6.5\ mm^2$) and reduced power consumption, which allow for system miniaturization and extended battery operation, respectively. It acts as the core of the presented instrument, with the embedded microcontroller programming and retrieving data from the AFE4900, implementing post-processing and transmitting acquired data to the host PC or Android device using the integrated BLE module. The inertial module is used to identify and remove motion artifacts.

Finally, a small and lightweight rechargeable lithium-ion polymer battery allows the FlexNIRS to be a wireless and wearable device that records data for more than 8 h.

More details of the hardware components, including part numbers, and the casing of the device are documented in the supplemental material.

2.3. Acquisition sequence - programming the AFE

To switch between 3 detectors and 4 LED sources we programmed the AFE to include four distinct periods. Each period includes 4 data collection phases and one data transfer phase. As shown in Fig. 3, during each of the periods 1, 3 and 4, a different detector is on, and the four LEDs are turned on in sequence one after another. In period 2 the LEDs are off to collect ambient light on the long separation (LS) detectors (D1 and D3).

The light intensity of individual LEDs is adjustable and kept the same across the three LED on periods. When switching between the short separation (SS) detector and LS detectors, the AFE is programmed by the BLE to change the TIA gain according to the numbers set by the user to compensate for the difference in light intensity.

As a default, we set the duration of each period to 2.5 ms. With 4 periods, it adds up to a full cycle length of 10 ms, i.e. a 100 Hz SO_2 acquisition rate. The 2.5 ms period includes 2.16 ms of data collection followed by data transfer. During the data collection phase, each LED is turned on for 336 μs. Each LED is turned on three times (336×3 = 1008 μs) throughout the four periods, resulting in 10% duty cycle. In this operating regime, the average light power is about 10 mW per LED at the maximum 200 mA forward current, well within American National Standards Institute (ANSI) safety standards. We can increase or decrease the acquisition rate by changing the duration of the 4 collection phases as needed by reprogramming AFE. High acquisition rates can be achieved at the expense of lower LED integration time, and hence lower SNR. We verified that 50, 100 and 130 Hz data acquisition rates provide sufficient SNR and are sustainable from a BLE data rate standpoint. These acquisition rates enable advanced measurement modes, including photoplethysmography and pulse oximetry, and permit several hours of battery-powered operation. The measurements in this paper are all performed at a 100 Hz sampling rate.

2.4. Bluetooth low energy protocol

BLE is a low-power wireless communication protocol that uses periodic connections with fixed connection interval. The throughput of BLE depends on several factors: the connection interval, the packet length, and the data-to-header ratio. We chose to use BLE 4.2 because it expands the data length (ATT_MTU) from 23 bytes to 247 bytes, improving the data-to-header ratio (Bulić et al., 2019).

In the current version, FlexNIRS uses a connection interval of 7.5 ms. To increase data throughput, the optical and acceleration data is transferred through the FlexNIRS initialized BLE notification, which does not require the client's (the mobile device) acknowledgement. Multiple notifications can be transferred within a connection interval. Contrarily, changing settings of detectors' gain and LEDs current is done through BLE write, an acknowledged data transfer requiring two connection intervals.

2.5. Hemoglobin oxygen saturation calculations

To obtain a robust SO_2 from a two-wavelength CW-NIRS system, we opted for a 2-distance symmetric geometry. In the diffuse regime, the light reflectance $\left(R \propto exp\left(-\sqrt{3\mu_a\mu_s}\right)/\rho^2\right)$ is a function of the source-detector separation distance (ρ) and the absorption and reduced

scattering coefficient (μ_a and μ_s') (Fantini et al., 1999; Liu et al., 1995). Thus, the slope of $\ln(\rho^2 \boldsymbol{R})$ vs. ρ is proportional to $-\sqrt{3\mu_a\mu_s'}$ (Matcher et al., 1995; Patterson et al., 1989). By assuming a known μ_s', we can solve for μ_a.

$$\mu_a(\lambda_i) = \frac{1}{3\mu_s'(\lambda_i)}\left[\frac{1}{\rho_1 - \rho_2}\ln\left(\frac{\rho_2{}^2\boldsymbol{R}(\rho_2, \lambda_i)}{\rho_1{}^2\boldsymbol{R}(\rho_1, \lambda_i)}\right)\right]^2 \quad (1)$$

Using a symmetric geometry, we can apply the self-calibrated method, for which the ratio of light reflectance between the two distances can be calculated regardless of the detectors and coupling efficiency, i.e. using different sources and detectors without the need for calibration (Hueber, 2000):

$$\frac{\boldsymbol{R}(\rho_2, \lambda_i)}{\boldsymbol{R}(\rho_1, \lambda_i)} = \sqrt{\frac{\boldsymbol{I}(\rho_2, s_{1\lambda_i}, d_2)\boldsymbol{I}(\rho_2, s_{2\lambda_i}, d_1)}{\boldsymbol{I}(\rho_1, s_{1\lambda_i}, d_1)\boldsymbol{I}(\rho_1, s_{2\lambda_i}, d_2)}}, \quad (2)$$

where $\boldsymbol{I}(\rho_i, s_j, d_k)$ is the light intensity detected from the source s_j and the detector d_k at a separation ρ_i. We will refer to only using Eq. (1) from here on as the non-self-calibrated method.

The hemoglobin oxygenation is then derived by solving the system of equations for the molar concentration of oxy- and deoxy-hemoglobin (HbO and HbR, respectively) (Shah et al., 2001), using the measured absorption at 2 wavelengths, the oxy- and deoxy- hemoglobin extinction coefficients (Prahl et al., 1998) and assuming a water fraction in the tissue (Hale and Querry, 1973).

The hemoglobin concentrations are then used to find the percent mole fraction of oxy-hemoglobin, i.e. the hemoglobin oxygen saturation,

$$SO_2 = \mathrm{HbO}/(\mathrm{HbO} + \mathrm{HbR}) \times 100\% . \quad (3)$$

In our device, for the calculations of SO_2 we used the LS detectors: 2.8 cm (LS1, S1 - D3 (ρ_{13}) and S2 - D1 (ρ_{21})) and 3.3 cm (LS2, S1 - D1 (ρ_{11}) and S2 - D3 (ρ_{23})) (Fig. 3 b). For the water fraction, we used 75% (Demel et al., 2014; Neeb et al., 2006; Selb et al., 2014), and for μ_s' we used 6.8 and 5.9 cm^{-1}at 735 and 850 nm, respectively. These scattering values were derived from the wavelength dependence exponential fit $\left(\mu_s' = 6.63(\lambda/750)^{-0.99}\right)$ from the young population in a previous study (Hallacoglu et al., 2012).

Errors in the assumption have some impact on SO_2, though we will show the impact in most cases is within a 5% uncertainty in SO_2 estimates. SO_2, being a ratio of concentrations, i.e. absorptions, depends more on the spectral features of the assumed scattering (the

exponential factor −0.99), than on its absolute values (Matcher et al., 1995). Regarding the water absorption, the % fraction assumption is only relevant for low hemoglobin concentrations, and negligible for typical concentration in brain tissue. Also, since the probe is flexible, when attached to the forehead, the distances can change slightly. This accounts for an error in SO_2 estimation only if the difference between the two separations is not maintained. In the result section, we report the effects of each of these parameters on SO_2.

The most relevant assumption we make is that the source-detector distances are symmetrically identical. While the source-detector symmetry is guaranteed on a flat surface, on the forehead the symmetry can be lost, which has a strong effect on the measured SO_2. To minimize the symmetry error, we have established a set of criteria and thresholds to detect when the symmetry is lost and the probe needs repositioning. Specifically, by considering the data from each source (2 wavelengths each) and two detectors independently, we expect:

- the light intensity ratios $R(\rho_{11})/R(\rho_{13})$ and $R(\rho_{23})/R(\rho_{21})$ to be within 0.05 – 0.8;
- the difference between the two intensity ratios to be less than 0.6;
- the difference between the two non-self-calibrated SO_2 of the two source locations (SO_{2S1} and SO_{2S2}) to be less than 100%.

The criteria and thresholds were determined in an initial group of 10 subjects, not presented here, acquiring data in several forehead locations. The reason for the large ranges in the criteria is that single source parameters are obtained without any calibration and thus are subject to components and light-coupling efficiency variation.

In addition, using the self-calibrating geometry we expect the absorption coefficients at the 2 wavelengths to be within physiological ranges:

- the self-calibrated absorption coefficients to be within 0.05–0.5 cm^{-1}.

2.6. FlexNIRS app

To maximize the portability of the oximeter, we developed a mobile app implementing a graphical user interface. The app was built on the Android 10 operating system and works with BLE protocol 4.2. It communicates with the device, visualizes the light intensity, cerebral oxygenation, and motion on the screen in real time, and saves the data on the device.

Upon connecting to the oximeter, the app opens four different tabs (“fragments” in Android), each with various features including real-time feedback that help the user optimize data quality and monitor results (Fig. S2). A banner is located on the top of the screen of all the tabs, allowing for easy access to essential functions: connect/disconnect to the FlexNIRS Bluetooth, start/stop data recording, log events, and a pop-up settings window to change assumed tissue scattering, water concentration, sources-detectors separations, and data quality thresholds. At the bottom of all the tabs, the values of the data quality parameters are displayed and followed by green/red dots to warn the user about detector saturation and aid correct probe positioning on the forehead. Screenshots of the mobile app tabs are shown in the supplemental material.

2.7. Device characterization and phantom measurement

2.7.1. Noise-equivalent power (NEP)—To measure NEP, we used two motorized 6-position neutral density filter wheels (FW102C, Thorlabs, USA) to attenuate the light to a series of 36 different levels (from no attenuation, OD 0, to OD 6). During the measurements, the light of one wavelength was output from one of the bicolor LEDs. The light was guided through the filter wheels and out to a detector through 2.5 mm fiber bundles. We removed background signals by subtracting the mean values of a 60 s dark measurement. We acquired 20 s of data for each of the 36 attenuation levels and repeated the measurements for the two wavelengths. To calculate the NEP of a bandwidth of 1 Hz, we segmented the signal into 0.5 s segments and determined the incident optical power required to obtain an SNR of 1 through linear fitting in the $\log_{10}$ scale.

2.7.2. Stability tests—The device's stability was evaluated by monitoring the detected light intensity over an extended acquisition time until the battery ran out. The FlexNIRS probe was secured on a solid silicon phantom, with optical properties mimicking biological tissue. We started the acquisition as soon the system was turned on with a full battery and acquired data until the 650 mAh battery was depleted. The current for all four LEDs was set to the maximum (200 mA). The voltage of the battery was sampled with an analog-to-digital converter at a sampling rate of 1 Hz.

2.7.3. Phantom's absorption coefficients—We used four tissue-like silicon phantoms of known optical properties to test the device's ability to retrieve the absorption coefficients, inputting the right reduced scattering coefficients. Each phantom was measured three times for 10 s each, and the results were compared with the known absorption values.

2.8. Human participant tests

To test the FlexNIRS in humans we enrolled and measured 5 healthy subjects (age range of 18–29, 1 male and 4 female, four light and one dark skin). The study was reviewed and approved by Mass General Brigham (MGB) Institutional Review Board. MGB IRB follows Ethical Principles and Guidelines for the Protection of Human Subjects (Belmont Report). All participants gave informed consent prior to the measurements. The measurement protocol included four tasks: probe-repositioning, hyperventilation, breath-holding, and walking/stair-climbing.

Probe-repositioning was done to evaluate SO_2 variability across the forehead. For this task we held the FlexNIRS probe in contact with the subject's forehead for 10 s and then moved to a new location on the forehead and repeated the measurement. In each subject we measured 6 distinct locations in the area between the hairline and the eyebrows, avoiding the midline, in either the left or right side of the forehead, as chosen randomly. During post-processing, each 10 s data acquired at a location was averaged at 1 Hz, and data points that did not meet the data quality criteria were discarded.

Hyperventilation and breath-holding were performed to perturb cerebral oxygenation. Hyperventilation causes hypocapnia, which leads to vessel constriction and a decrease in cerebral blood flow, resulting in a subsequent decrease in SO_2 (Wilson et al., 1991). Breath-

holding reduces oxygen availability and thus lowers SO_2. During these tasks, in addition to the FlexNIRS, we used a commercial frequency domain near-infrared spectroscopy (FD-NIRS) device (MetaOx, ISS Inc.) (Carp et al., 2017) to simultaneously measure SO_2. The FD-NIRS recovers optical properties by using a multi-distance scheme (1.5, 2, 2.5 and 3 cm source-detector separations) and was calibrated in 2 silicon phantoms. To avoid crosstalk between the two devices, the optical probes were positioned on the opposite sides of the forehead. For hyperventilation, after a 60 s baseline, the subjects were instructed to breathe at a rate of 70 breaths per minute followed by 2 min of rest. The task was repeated twice. For breath-holding, after a 60 s baseline, the subjects held their breath for 25 s and then breathed regularly for 45 s. The task was repeated three times. Each breath-hold was initialized with an exhalation (Meyer et al., 1966). During these tasks, we also acquired pulse oximetry signals and respiration signals with a physiological data acquisition system (BIOPAC system Inc.) to ensure subject compliance.

Walking/stair-climbing tasks were performed to assess the sensitivity to motion of the FlexNIRS. During this task, the subject with the FlexNIRS secured on the forehead walked through a hallway, climbed up 4 flights of stairs, then walked back down the stairs and the hallway back to the testing room where they rested for 1 min. The heart rate was calculated from the FlexNIRS data by identifying the peaks of the pulsatile light intensity filtered with a low-pass infinite-impulse-response zero-phase digital filter (passband of 14.5 Hz, stopband of 15.5 Hz, passband ripple of 1 dB and stopband attenuation of 60 dB). The peaks were then identified with a custom heartbeat-locating algorithm and the inverse of the duration between neighboring peaks was considered to be the heart rate. A moving median of 15 heartbeats was applied to reject outliers due to motion artifacts.

Saved raw data were re-analyzed with Matlab to verify consistency with the app-saved results. FD-NIRS and auxiliary data from the MetaOx device were also analyzed with custom scripts. For these comparisons, we used fixed reduced scattering coefficients for the FlexNIRS (6.8 and 5.9 cm^{-1} at 735 and 850 nm) and the measured scattering coefficients for the FD-NIRS. To examine how source-detector separation, water concentration and scattering affect the calculated SO_2 in humans, we analyzed the experimental data with manipulated separations, water content and reduced scattering coefficients. Specifically, we tested the effect of multiplying and adding a constant to all separations, the effect of the different spectral dependences of the assumed reduced scattering coefficients, and the effect of different water concentrations.

2.9. Data and code availability statement

As stated previously, we are making this device open source. The hardware (circuit schematic and 3D drawing) and the software files are available on https://optics.martinos.org/flexnirs/ for non-commercial use. The data will be made available upon contact with the authors.

3. Results

3.1. Noise equivalent power

Fig. 4 shows the NEP of the device at 735 and 850 nm. Using the default acquisition conditions we measured an NEP of 66.4 fW/ √Hz at 735 nm and 57.9 fW// √Hz at 850 nm.

3.2. Stability measurement

Using the maximum light intensity output and starting with a full battery, the FlexNIRS lasted 8 h and 5 min. Thwite initial battery voltage was 4.17 V and the device stopped when the battery reached 3.00 V. The optical data acquired in a tissue-like silicon phantom and the battery voltage are reported in Fig. 5 with averaging of 1 point per minute. After an initial 60 min warm up, during which the intensity changed 3, 4%, for the next several hours, the intensity remained near-constant with a maximum deviation of 1% despite the steady drop in battery voltage.

Throughout the measurement, the self-calibrated R_{LS2}/R_{LS1} (Eq. (2)) remains close to constant (change of −0.3% to 0.4%); when considering the data from each source independently, the intensity ratios $R(\rho_{11})/R(\rho_{13})$ and $R(\rho_{23})/R(\rho_{21})$ showed larger variations (change of −1.9% to 2.8%). The stability of the intensity ratios and derived parameters is an advantage of the self-calibrated method, which is not affected by the detector nor the source efficiency variation over time. Similarly, as expected, the self-calibrated μ_a varied between −0.8% and 0.6%, whereas the non-self-calibrated μ_a varied between −5.2% and 3.9%. The apparent SO_2 of the silicon phantom changed only 0.7% during the whole measurement.

3.3. Phantom measurement

Fig. 6 reports the absorption coefficient results on the four tissue-like silicon phantoms with respect to the known absorption coefficients (previously measured with a FD-NIRS system). The FlexNIRS self-calibrated measured μ_a correlated well with the known values, with an R^2 of 0.93 (slope of 1.1, $p = 2.1 \times 10^{-26}$). The Bland-Altman analysis shows bias of −0.008 cm^{-1} and standard deviation of 0.01 cm^{-1}.

3.4. Human tests

The high acquisition rate (100 Hz) and the high SNR of the FlexNIRS allowed us to resolve arterial pulsation at all separations. In Fig. 7 we show raw light intensity signals for 6 out of 12 channels (S1 and D1, D2, D3) acquired on a representative subject on a short timescale, to highlight the detected arterial pulsation signals. The arterial pulsation is clear in the raw signals even at 3.3 cm separation without the need of any averaging or filtering. The arterial pulsation is also visible in the measured SO_2 which is also derived at 100 Hz.

3.5. Probe positioning

Fig. 8 shows boxplots of the SO_2 results for the 5 subjects. Markers of different colors indicate different locations. In two subjects we successfully measured only 5 locations given that all the points in one of the 6 locations did not meet quality criteria. While across subjects the range of SO_2 is relatively large, within-subjects SO_2 varies between 6.1% and

11.6% across the forehead. As a comparison, using a single source geometry provides a much greater variability in SO_2.

3.6. Hyperventilation and breath-holding

Fig. 9 shows SO_2 time traces during hyperventilation and breath-holding in a representative subject. As expected, hyperventilation SO_2 decreased and recovered after normal breathing was resumed. During breath-holding, we observed small increases in SO_2 followed by a decrease. The trends of the two devices matched relatively well; still, changes in SO_2 caused by the tasks were in general larger with the FlexNIRS than with the FD-NIRS. This could be due to the different probe locations and larger source-detector separations of the Flex-NIRS (2.8–3.3 cm) than for the FD-NIRS (1.5–3 cm). Fig. 9 also reports the scatter plot and the Bland-Altman plot of SO_2 measured with the FlexNIRS and the FD-NIRS in 4 subjects. Data from the first subject were excluded due to extremely low oxygenation measured by the FD-NIRS device (avg. resting SO_2 of 34.8%, vs. 49.7% with the FlexNIRS). The correlation coefficient is $R^2 = 0.59$ and $p < 0.001$, the bias is −1.97% and the standard deviation is 2.7%; 95.3% of the data points fell within the ±1.96 standard deviation range. These results show good agreement of the FlexNIRS SO_2 with the gold standard FD-NIRS, and low sensitivity to scattering of the SO_2 measurement. In fact, the reduced scattering coefficients measured with the FD-NIRS were 59.8 ± 22.2% higher in value and 21.7% ± 49.7% higher in power slope compared to the assumed scattering on the FlexNIRS calculation and varied across subjects, whereas the differences in SO_2 between the two methods have ±1.96 standard deviation range of +3.37%—7.32%, similar to the variation we measured across different forehead locations.

3.7. Walking and stair-climbing

During walking and climbing stairs, the FlexNIRS measured SO_2 did not show significant motion artifacts. SO_2 time traces (blue, left *y*-axis), heart rate FlexNIRS estimates (red, right *y*-axis) and acceleration measured by the FlexNIRS accelerometer (yellow, right *y*-axis) for all 5 subjects are reported in Fig. 10. Changes in SO_2 during walking/climbing were in general small and subject-dependent. Heart rate in all subjects increased during the stairs ascending period and recovered during the stairs descending period.

3.8. Sensitivity to assumed parameters

To understand how the assumed parameters affect the accuracy in SO_2, in the human data we artificially changed the input parameters, including source-detector separations, reduced scattering coefficient and percentage of water, within physiological ranges. The calculation was performed on the 60 s initial baseline of the two hyperventilation and the three breath-holding tasks of the 5 subjects. For each measurement, the 60 s SO_2 baseline was averaged into one datapoint, and for each parameter, the average and standard deviation across the 15 measurements were calculated. SO_2 estimated using default parameters was 56.4% ± 5.2% (average ± standard deviation).

Changing source-detector separation values: Adding or subtracting 1 mm to all source-detectors separations had no effect on SO_2; doing so by 4 mm results in an SO_2 increase of 0.34% or decrease of 0.54%, respectively. Multiplying the separations by a factor of 0.8 or 1.2 (20% change) caused SO_2 to increase by 1.8% or decrease by 2.6%, respectively. We also examined the effect of varying one of the two long separations (2.8 and 3.3 cm). Adding or subtracting 1 mm to LS1 resulted in an SO_2 decrease of 1.3% or increase of 1%, respectively (doing so on LS2 causes the same changes but with opposite signs). Modifying only the separation of one wavelength is not possible since the LEDs are colocalized.

Changing assumed reduced scattering values: Adding or subtracting 1.5 cm^{-1} to μ_s' at both wavelengths resulted in an SO_2 increase of 5.4% or decrease of 4%, respectively. Multiplying μ_s' by 0.6 or 1.4 (40% change) resulted in an SO_2 increase of 2.1% or decrease of 2.2%. Multiplying the scattering exponential term (−0.99) by a factor of 0.6 or 1.4 resulted in an SO_2 decrease of 5.6% or increase of 3.2%, respectively.

Water fraction assumption: Changing the assumed percentage of water in tissue from the default value of 75% to 50% or 100%, changed SO_2 by 1.7% and −1.9%, respectively, showing that the accuracy of the water percentage assumption has little impact on the accuracy of SO_2.

Each of these changes is within $a \pm 5.6\,\%$ error. To estimate the combined effect, we assumed the three sources of error to be independent of each other and the error to have a normal distribution. We calculated the cumulative error to be $\pm 6.2\,\%$ in SO_2 estimates.

4. Discussion

We have developed and built a low-cost, wireless, and wearable cerebral oximeter that meets all the key requirements for a personalized cerebral health tracker for use in the general population (listed in the introduction).

The choice of CW-NIRS allowed us to build the device at a low cost. The current cost for 50 FlexNIRS units is about $200 per unit, mostly due to the cost of PCB manufacturing and assembly. Scaling up to 1000 units, the cost is reduced to ~$50 per unit (based on US electronic component retailer pricing). While CW-NIRS is inherently less accurate than FD-NIRS or time-domain (TD) NIRS, and the scattering assumption prevents absolute quantification of hemoglobin concentrations, the goal to accurately quantify SO_2 via CW-NIRS is achievable as we have verified that an inaccurate scattering assumption does not affect SO_2 estimates by more than 5%. This is within the SO_2 variability we have observed across different locations on the forehead and less than the variability across subjects measured with the FD-NIRS. In addition to lowering the cost, the use of CW rather than FD- or TD-NIRS provides a much better SNR at our desired sampling rate (Davies et al., 2017). The low NEP achieved is remarkable for a wearable NIRS device, and this is mostly thanks to the noise performance of the integrated AFE circuit. While the complex logic structure of the AFE may pose constraints and limit its flexibility for different applications, it is well

suited for cerebral oximetry, as one can take advantage of the superior noise performance with respect to other controllers which need external amplification.

The circuit's modular approach, low profile, and lightweight design, along with the choice of a flexible PCB for the probe module and comfortable headband design, lead to good device wearability. In fact, the FlexNIRS was well-received by all subjects who performed walking tasks with no constraints.

Moreover, the battery operation and Bluetooth communication with an Android tablet provided complete freedom of movement and maintained a strong connection within 10–20 m. Mild loss of datapoints was observed when using the FlexNIRS near large metal objects or when simultaneously using other Bluetooth devices (e.g. an iPhone actively communicating with an Apple watch). The rechargeable battery had a battery life of 8 h when the FlexNIRS LEDs were turned on at maximum power, and FlexNIRS provided very stable SO_2 to the very end of the battery life. We verified that we could use single-use AAA batteries to achieve equivalent performance.

We also verified that casing FlexNIRS inside a 3D printed headband with Velcro straps provides good contact with the skin and shields the detectors from ambient light. To further increase stability and light blockage, a second fabric headband was used while walking through the well-lit hallways and climbing stairs. This resulted in the acquisition of a very stable SO_2 while performing activities, demonstrated by being able to quantify heart rate from the acquired intensity signals. In addition, an inertial module mounted on the BLE module allows for the detection and rejection of periods of head motion, as needed.

Using the multi-distance self-calibrating geometry, we were able to obtain cerebral oxygenation values comparable to FD-NIRS without the need for any calibration. We believe this self-calibrating method is key for the robust quantification of SO_2 without the need for proprietary algorithms used by commercial cerebral oximeters. The long-term stability test against light intensity drifts (Fig. 5) showed deviations smaller than a few percent. The probe-repositioning test showed that the self-calibrating method resulted in much higher reproducibility than the single-LED geometry. Nevertheless, we should note that the single-LED geometry in this study is not identical to traditional linear geometry. The two detectors are not on the same linear trajectory away from the detector—the paths the photons travel overlap less than in traditional linear geometry and thus intrinsically may introduce larger errors.

Our SO_2 estimates, as in commercial cerebral oximeters, are affected by scalp and skull contamination. While a possible future expansion will be to use the short separation as a regressor to minimize scalp contamination, as is done in fNIRS (Gagnon et al., 2011; Saager and Berger, 2008; Sato et al., 2016; von Lühmann et al., 2020; Yücel et al., 2015), to estimate SO_2 we currently only rely on the use of large separations (2.8 and 3.3 cm) and a multi-distance scheme. The multi-distance approach is less sensitive to scalp hemoglobin changes than a single-distance method (Fantini et al., 1999).

Currently, the short source-detector separation is used to quantify heart rate. In future developments, in addition to being used for scalp contamination reduction, the short separation will be used to quantify reflectance photoplethysmography (rPPG) (Longmore et al., 2019) and heart rate variability (Georgiou et al., 2018).

Finally, the app-based acquisition and data analysis software provides real-time feedback and alerts and allowed for remote monitoring. The development of data quality criteria allowed us to immediately identify poor positioning of the probe and obtain robust SO_2 values in good agreement with state-of-the-art FD-NIRS.

Human subject data during breathing tasks demonstrated the ability of the device to consistently detect small changes in SO_2. This was better shown by the hyperventilation experiments than the breath-holding experiments. One reason is that during hyperventilation, the induced hypocapnia leads to vessel constriction and a decrease in cerebral blood flow (Raichle and Plum, 1972; Reivich, 1964). The breath-holding duration (25 s) may be too short to induce large drops in cerebral oxygenation, since in the first 30–50 s of breath-holding, the reduced oxygen content in the blood is counteracted by an increase in cerebral blood flow (Bouten et al., 2020; Ozana et al., 2021; Settakis et al., 2002).

The breathing tasks demonstrate the sensitivity of the FlexNIRS device to small changes in SO_2, and the stairs climbing task shows the ability to perform these measurements while freely moving. The FlexNIRS is well suited for daily cerebral oxygenation measurements outside the hospital and the laboratory settings. Among the many applications, one can think of using this device as a home monitor to detect apnea-hypopnea events for sleep apnea, or to detect cerebral hypoxia due to Covid 19 or other diseases affecting cerebral perfusion.

5. Conclusion

We have successfully realized a wireless CW-NIRS cerebral oximeter called FlexNIRS. The device was able to quantify SO_2 at 100 Hz using multi-distance CW-NIRS with a self-calibrating probe design. Through validation using optical phantoms and human measurements, the device has proven to be a reliable, low-cost alternative for SO_2 quantification. The device performance shows low noise and robustness against signal drifts and everyday motion. The low cost and long battery life allow for prolonged monitoring. We are making this device open source to allow researchers worldwide to test and demonstrate its utility to monitor brain health.

Supplementary Material

Refer to Web version on PubMed Central for supplementary material.

Funding sources

This work was supported by Maria Angela Franceschini's Sundry fund and by the National Institutes of Health [R21AG072481, R01HD091067, R01GM116177].

Data and code availability statement

As stated previously, we are making this device open source. The hardware (circuit schematic and 3D drawing) and the software files are available on https://optics.martinos.org/flexnirs/ for non-commercial use. The data will be made available upon contact with the authors.

Abbreviations

ADC	analog-to-digital converter
AFE	analog front-end
ANSI	American National Standards Institute
BLE	Bluetooth Low Energy
CW	continuous wave
ECG	electrocardiogram
FD	frequency domain
HbO	oxyhemoglobin
HbR	deoxyhemoglobin
HR	heart rate
IR	infrared
LED	light-emitting diode (common abbreviation)
LS	long separation
μ_a	absorption coefficient
μ_s	reduced scattering coefficient
NEP	noise-equivalent power
NIRS	near-infrared spectroscopy
PCB	printed circuit board
R	reflectance
ρ	source-detector separation
SiP	system-in-package
SNR	signal-to-noise ratio
SO_2	hemoglobin oxygen saturation

SpO_2	pulse oximetry peripheral capillary oxygen saturation
SS	short separation
TD	time domain
TIA	transimpedance amplifier

References

Benni PB, MacLeod D, Ikeda K, Lin HM, 2018. A validation method for near-infrared spectroscopy based tissue oximeters for cerebral and somatic tissue oxygen saturation measurements. J. Clin. Monit. Comput 32 (2), 269–284. [PubMed: 28374103]

Bouten J, Bourgois JG, Boone J, 2020. Hold your breath: peripheral and cerebral oxygenation during dry static apnea. Eur. J. Appl. Physiol 120 (10), 2213–2222. [PubMed: 32748010]

Buekers J, Theunis J, De Boever P, Vaes AW, Koopman M, Janssen EVM, Wouters EFM, Spruit MA, Aerts JM, 2019. Wearable finger pulse oximetry for continuous oxygen saturation measurements during daily home routines of patients with chronic obstructive pulmonary disease (COPD) over one week: observational study. JMIR mhealth uhealth 7 (6), e12866.

Bulić P, Kojek G, Biasizzo A, 2019. Data transmission efficiency in bluetooth low energy versions. Sensors 19 (17), 3746. [PubMed: 31470669]

Carp SA, Farzam P, Redes N, Hueber DM, Franceschini MA, 2017. Combined multi-distance frequency domain and diffuse correlation spectroscopy system with simultaneous data acquisition and real-time analysis. Biomed. Opt. Express 8 (9), 3993. doi: 10.1364/boe.8.003993. [PubMed: 29026684]

Davies DJ, Clancy M, Lighter D, Balanos GM, Lucas SJE, Dehghani H, Su Z, Forcione M, Belli A, 2017. Frequency-domain vs continuous-wave near-infrared spectroscopy devices: a comparison of clinically viable monitors in controlled hypoxia. J. Clin. Monit. Comput 31 (5), 967–974. [PubMed: 27778208]

Demel A, Wolf M, Poets CF, Franz AR, 2014. Effect of different assumptions for brain water content on absolute measures of cerebral oxygenation determined by frequency-domain near-infrared spectroscopy in preterm infants: an observational study. BMC Pediatr. 14 (1), 1–6. [PubMed: 24387002]

Fantini S, Hueber D, Franceschini MA, Gratton E, Rosenfeld W, Stubblefield PG, Maulik D, Stankovic MR, 1999. Non-invasive optical monitoring of the newborn piglet brain using continuous-wave and frequency-domain spectroscopy. Phys. Med. Biol 44 (6), 1543–1563. doi: 10.1088/0031-9155/44/6/308. [PubMed: 10498522]

Fuller D, Colwell E, Low J, Orychock K, Tobin MA, Simango B, Buote R, Van Heerden D, Luan H, Cullen K, 2020. Reliability and validity of commercially available wearable devices for measuring steps, energy expenditure, and heart rate: systematic review. JMIR mhealth uhealth 8 (9), e18694.

Gagnon L, Perdue K, Greve DN, Goldenholz D, Kaskhedikar G, Boas DA, 2011. Improved recovery of the hemodynamic response in diffuse optical imaging using short optode separations and state-space modeling. Neuroimage 56 (3), 1362–1371. doi: 10.1016/j.neuroimage.2011.03.001. [PubMed: 21385616]

Georgiou K, Larentzakis AV, Khamis NN, Alsuhaibani GI, Alaska YA, Giallafos EJ, 2018. Can wearable devices accurately measure heart rate variability? A systematic review. Folia Med. 60 (1), 7–20.

Green MS, Sehgal S, Tariq R, 2016. Near-infrared spectroscopy: the new must have tool in the intensive care unit? Semin. Cardiothorac. Vasc. Anesth 20 (3), 213–224. [PubMed: 27206637]

Hale GM, Querry MR, 1973. Optical constants of water in the 200-nm to 200-μm wavelength region. Appl. Opt 12 (3), 555–563. [PubMed: 20125343]

Hallacoglu B, Sassaroli A, Fantini S, Wysocki M, Guerrero-Berroa E, Beeri MS, Haroutunian V, Shaul M, Rosenberg IH, Troen A, 2012. Absolute measurement of cerebral optical coefficients,

hemoglobin concentration and oxygen saturation in old and young adults with near-infrared spectroscopy. J. Biomed. Opt 17 (8), 81406.

Hogue CW, Levine A, Hudson A, Lewis C, 2021. Clinical applications of near-infrared spectroscopy monitoring in cardiovascular surgery. Anesthesiology 134 (5), 784–791. [PubMed: 33529323]

Huang CY, Chan MC, Chen CY, Lin BS, 2014. Novel wearable and wireless ring-type pulse oximeter with multi-detectors. Sensors 14 (9), 17586–17599. [PubMed: 25244586]

Johnston WS, Mendelson Y, 2004. Extracting breathing rate information from a wearable reflectance pulse oximeter sensor. In: Proceedings of the 26th Annual International Conference of the IEEE Engineering in Medicine and Biology Society, 2, pp. 5388–5391.

Kim J, Gutruf P, Chiarelli AM, Heo SY, Cho K, Xie Z, Banks A, Han S, Jang K, Lee JW, 2017. Miniaturized battery-free wireless systems for wearable pulse oximetry. Adv. Funct. Mater 27 (1), 1604373.

Liu H, Boas DA, Zhang Y, Yodh AG, Chance B, 1995. Simplified approach to characterize optical properties and blood oxygenation in tissue using continuous near-infrared light. In: Proceedings of the Optical Tomography, Photon Migration, and Spectroscopy of Tissue and Model Media: Theory, Human Studies, and Instrumentation, 2389, pp. 496–502. doi: 10.1117/12.209998 May 1995.

Longmore SK, Lui GY, Naik G, Breen PP, Jalaludin B, Gargiulo GD, 2019. A comparison of reflective photoplethysmography for detection of heart rate, blood oxygen saturation, and respiration rate at various anatomical locations. Sensors (8) 19. doi: 10.3390/s19081874, (Switzerland).

Matcher SJ, Kirkpatrick PJ, Nahid K, Cope M, Delpy DT, 1995. Absolute quantification methods in tissue near-infrared spectroscopy. In: Proceedings of the Optical Tomography, Photon Migration, and Spectroscopy of Tissue and Model Media: Theory, Human Studies, and Instrumentation, 2389, pp. 486–495.

Meyer JS, Gotoh F, Takagi Y, Kakimi R, 1966. Cerebral hemodynamics, blood gases, and electrolytes during breath-holding and the Valsalva maneuver. Circulation 33 (5s2), II–35.

Neeb H, Zilles K, Shah NJ, 2006. Fully-automated detection of cerebral water content changes: study of age- and gender-related H_2O patterns with quantitative MRI. Neuroimage 29 (3), 910–922. doi: 10.1016/j.neuroimage.2005.08.062. [PubMed: 16303316]

Ozana N, Zavriyev AI, Mazumder D, Robinson MB, Kaya K, Blackwell MH, Carp SA, Franceschini MA, 2021. Superconducting nanowire single-photon sensing of cerebral blood flow. Neurophotonics 8 (3), 1–14. doi: 10.1117/1.NPh.8.3.035006.

Patterson MS, Schwartz E, Wilson BC, 1989. Quantitative reflectance spectrophotometry for the noninvasive measurement of photosensitizer concentration in tissue during photodynamic therapy. In: Proceedings of the Photodynamic Therapy: Mechanisms, 1065, pp. 115–122.

Pimentel MAF, Charlton PH, Clifton DA, 2015. Probabilistic estimation of respiratory rate from wearable sensors. In: Wearable Electronics Sensors. Springer, pp. 241–262.

Pinti P, Aichelburg C, Gilbert S, Hamilton A, Hirsch J, Burgess P, Tachtsidis I, 2018. A review on the use of wearable functional near-infrared spectroscopy in naturalistic environments. Jpn. Psychol. Res 60 (4), 347–373. [PubMed: 30643322]

Piper SK, Krueger A, Koch SP, Mehnert J, Habermehl C, Steinbrink J, Obrig H, Schmitz CH, 2014. A wearable multi-channel fNIRS system for brain imaging in freely moving subjects. Neuroimage 85, 64–71. doi: 10.1016/j.neuroimage.2013.06.062. [PubMed: 23810973]

Pollard V, Prough DS, DeMelo AE, Deyo DJ, Uchida T, Stoddart HF, 1996. Validation in volunteers of a near-infrared spectroscope for monitoring brain oxygenation *in vivo*. In: Anesth. Analg, 82, pp. 269–277. [PubMed: 8561326]

Hueber DM (2000). Self referencing photosensor (U.S. Patent No. 6,078,833). U.S. Patent and Trademark Office.

Prahl S, Gratzer WB, Kollias N, 1998. Tabulated molar extinction coefficient for hemoglobin in water. Oregon Medical Laser Center.

Raichle ME, Plum F, 1972. Hyperventilation and cerebral blood flow. Stroke 3 (5), 566–575. [PubMed: 4569138]

Reivich M, 1964. Arterial PCO_2 and cerebral hemodynamics. Am. J. Physiol. Leg. Content 206 (1), 25–35.

Rwei AY, Lu W, Wu C, Human K, Suen E, Franklin D, Fabiani M, Gratton G, Xie Z, Deng Y, 2020. A wireless, skin-interfaced biosensor for cerebral hemodynamic monitoring in pediatric care. Proc. Natl. Acad. Sci 117 (50), 31674–31684. [PubMed: 33257558]

Saager RB, Berger AJ, 2008. Measurement of layer-like hemodynamic trends in scalp and cortex: implications for physiological baseline suppression in functional near-infrared spectroscopy. J. Biomed. Opt 13 (3), 34017.

Sato T, Nambu I, Takeda K, Aihara T, Yamashita O, Isogaya Y, Inoue Y, Otaka Y, Wada Y, Kawato M, Sato Maki, Osu, R., 2016. Reduction of global interference of scalp-hemodynamics in functional near-infrared spectroscopy using short distance probes. Neuroimage 141, 120–132. doi: 10.1016/j.neuroimage.2016.06.054. [PubMed: 27374729]

Selb J, Boas DA, Chan ST, Evans KC, Buckley EM, Carp SA, 2014. Sensitivity of near-infrared spectroscopy and diffuse correlation spectroscopy to brain hemodynamics: simulations and experimental findings during hypercapnia. Neurophotonics 1 (1), 015005. doi: 10.1117/1.NPh.1.1.015005.

Seneviratne S, Hu Y, Nguyen T, Lan G, Khalifa S, Thilakarathna K, Hassan M, Seneviratne A, 2017. A survey of wearable devices and challenges. IEEE Commun. Surv. Tutor 19 (4), 2573–2620.

Settakis G, Lengyel A, Molnár C, Bereczki D, Csiba L, Fülesdi B, 2002. Transcranial Doppler study of the cerebral hemodynamic changes during breath-holding and hyperventilation tests. J. Neuroimaging 12 (3), 252–258. [PubMed: 12116744]

Shah N, Cerussi A, Eker C, Espinoza J, Butler J, Fishkin J, Hornung R, Tromberg B, 2001. Noninvasive functional optical spectroscopy of human breast tissue. Proc. Natl. Acad. Sci 98 (8), 4420–4425. [PubMed: 11287650]

Singh G, Tee A, Trakoolwilaiwan T, Taha A, Olivo M, 2020. Method of respiratory rate measurement using a unique wearable platform and an adaptive optical-based approach. Intensive Care Med. Exp 8, 1–10. [PubMed: 31897796]

von Lühmann A, Ortega-Martinez A, Boas DA, Yücel MA, 2020. Using the general linear model to improve performance in fNIRS single trial analysis and classification: a perspective. Front. Hum. Neurosci 14, 30. doi: 10.3389/fnhum.2020.00030, February. [PubMed: 32132909]

Wilson DF, Pastuszko A, DiGiacomo JE, Pawlowski M, Schneiderman R, Delivoria-Papadopoulos M, 1991. Effect of hyperventilation on oxygenation of the brain cortex of newborn piglets. J. Appl. Physiol 70 (6), 2691–2696. [PubMed: 1909316]

Yücel MA, Selb J, Aasted CM, Petkov MP, Becerra L, Borsook D, Boas DA, 2015. Short separation regression improves statistical significance and better localizes the hemodynamic response obtained by near-infrared spectroscopy for tasks with differing autonomic responses. Neurophotonics 2 (3), 35005.

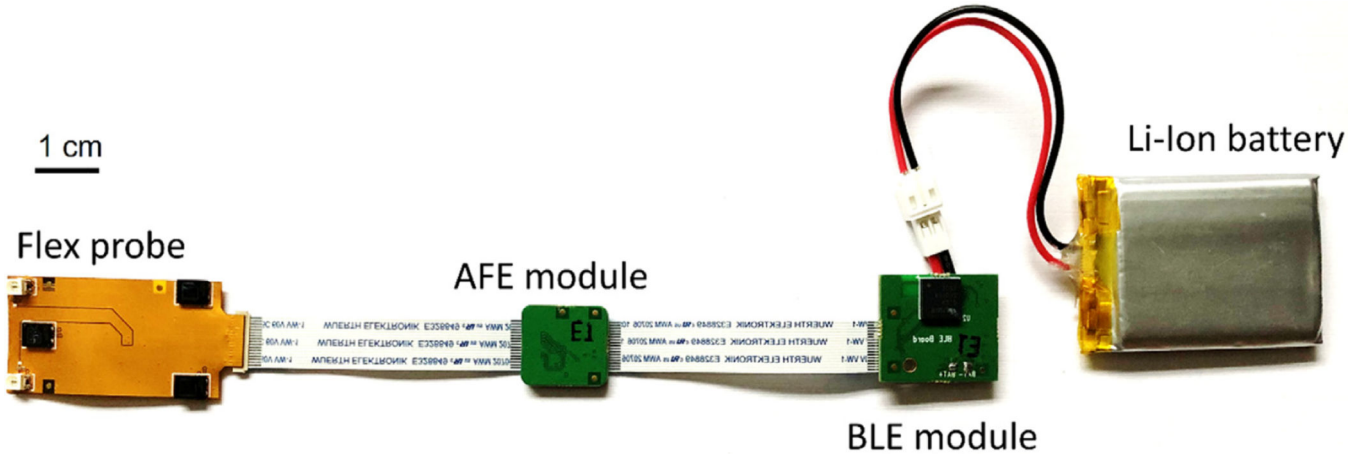

Fig. 1.

Prototype for a low-cost, wireless and wearable cerebral oximeter. The flex probe hosts the LEDs and the photodetectors on a flexible PCB. The AFE module controls and samples the optical signals. The BLE module enables wireless connection with a computer or a mobile device.

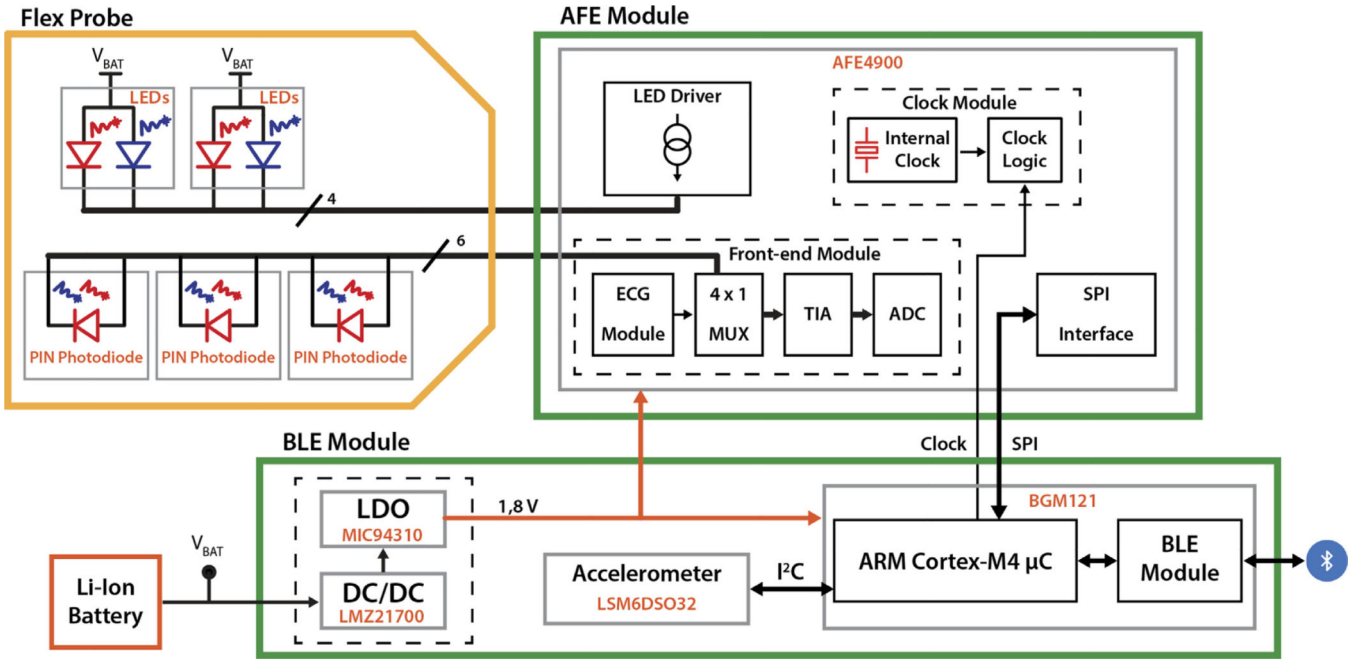

Fig. 2.
Simplified block diagram of the instrument.

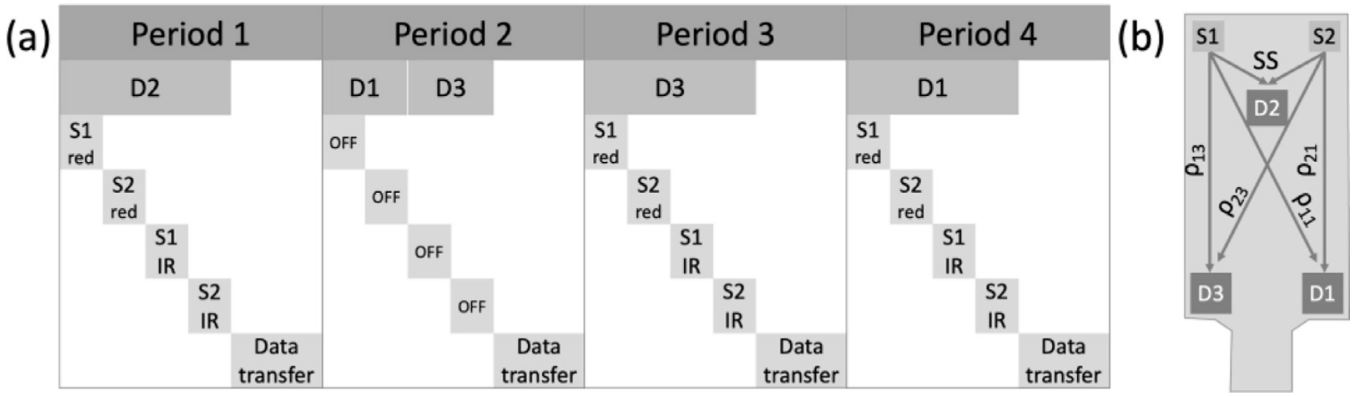

Fig. 3.

(a) Data acquisition sequence and FlexNIRS probe geometry. One acquisition cycle includes four 2.5 ms periods, each period including a data collection phase and a data transfer phase. In period 1, during the data collection phase the short separation detector (D2) is on and kept at a relatively low gain to avoid saturation, and the four LEDS are turned on in sequence for 336 μs each. In period 2, the detectors' gain is increased, and the data collection phase is split between detectors 1 and 3 while the LEDs are kept off to acquire ambient light. During periods 3 and 4 the long separation detectors (D3 and D1) are on at the same gain as in phase 2, and the LEDs are switched on in sequence as in period 1. A full cycle takes 10 ms. (b) Schematic drawing of the flex probe geometry. S1 and S2 both have two LEDs emitting light at 735 nm (red) and 850 nm (IR). D2 is the short separation (SS) detector at 0.8 cm from S1 and S2. D1 and D3 are the long separation detectors with distances ρ_{13} and ρ_{21} of 2.8 cm (LS1), and ρ_{11} and ρ_{23} of 3.3 cm (LS2) from the sources.

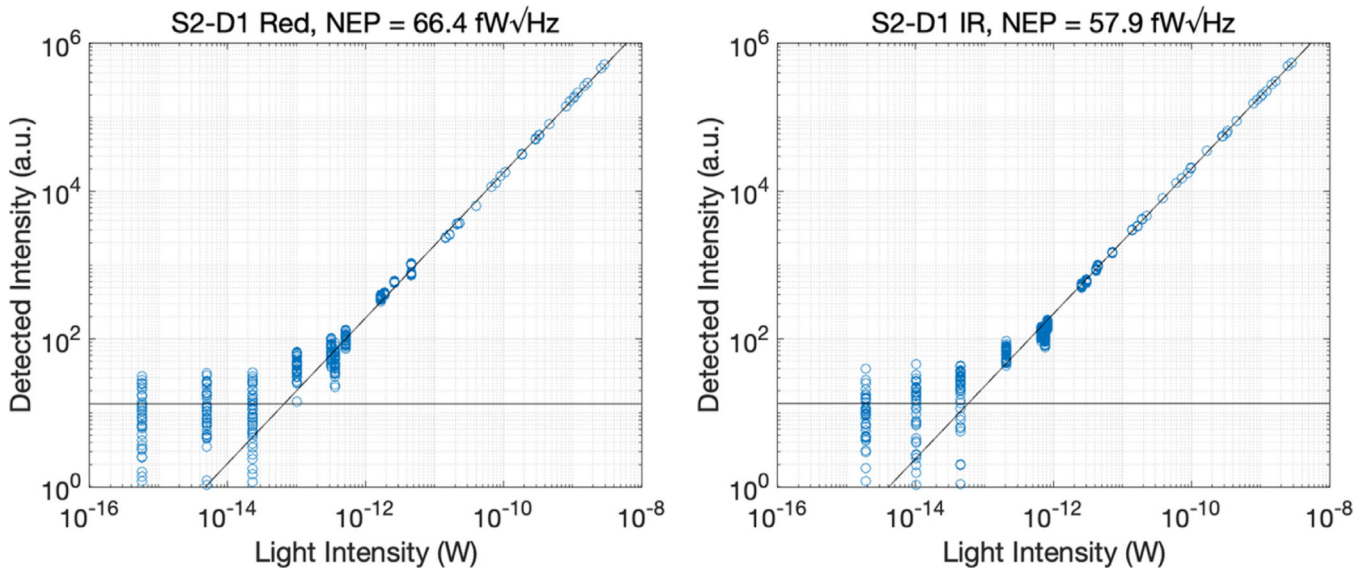

Fig. 4.

Scatterplot between detected and incident light at 735 nm (left panel) and 850 nm (right panel).

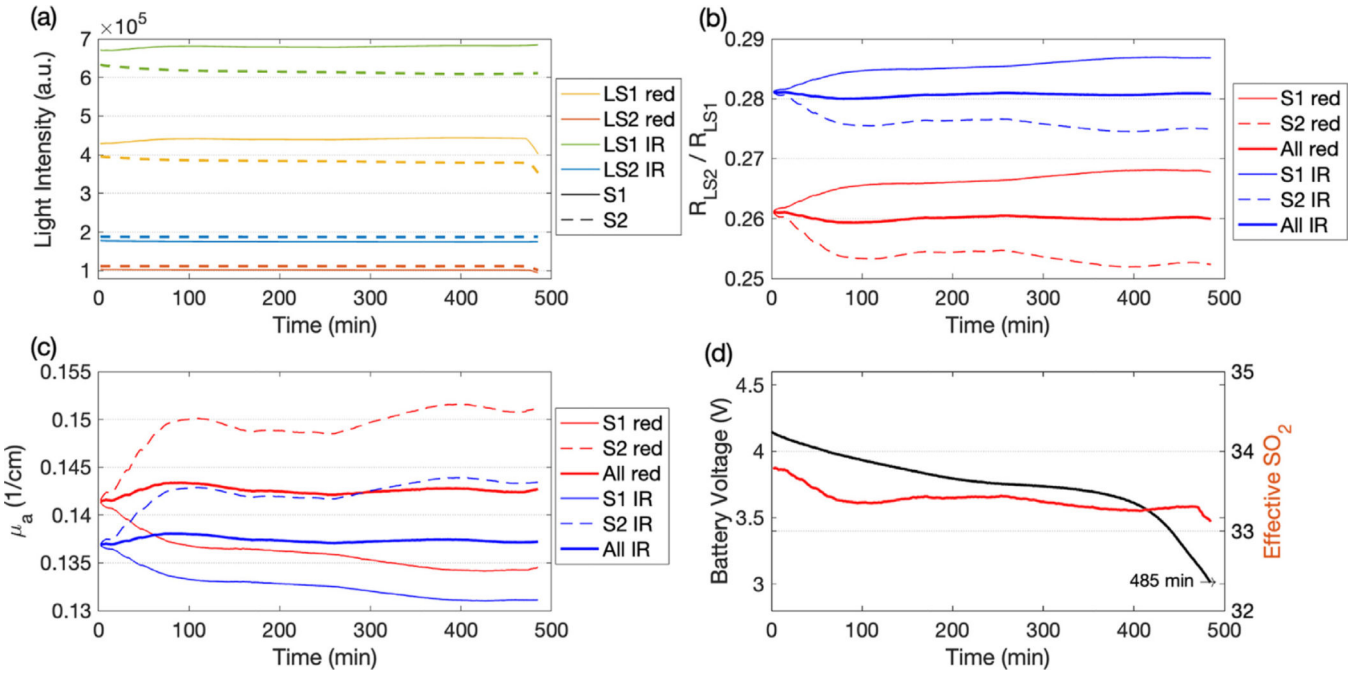

Fig. 5.

Stability test results during the 8 h battery life. (a) Light intensity at large separations, (b) reflectance ratios, (c) absorption coefficients, and (d) battery voltage (left y-axis, black) and self-calibrated SO_2 (right y-axis, red). In the legends LS1 is 2.8 cm, LS2 is 3.3 cm, red is 735 nm, IR is 850 nm, S1 indicates calculation obtained using source 1 (solid lines), S2 using source 2 (dashed lines) and All (thicker lines) using both sources with the self-calibrated method.

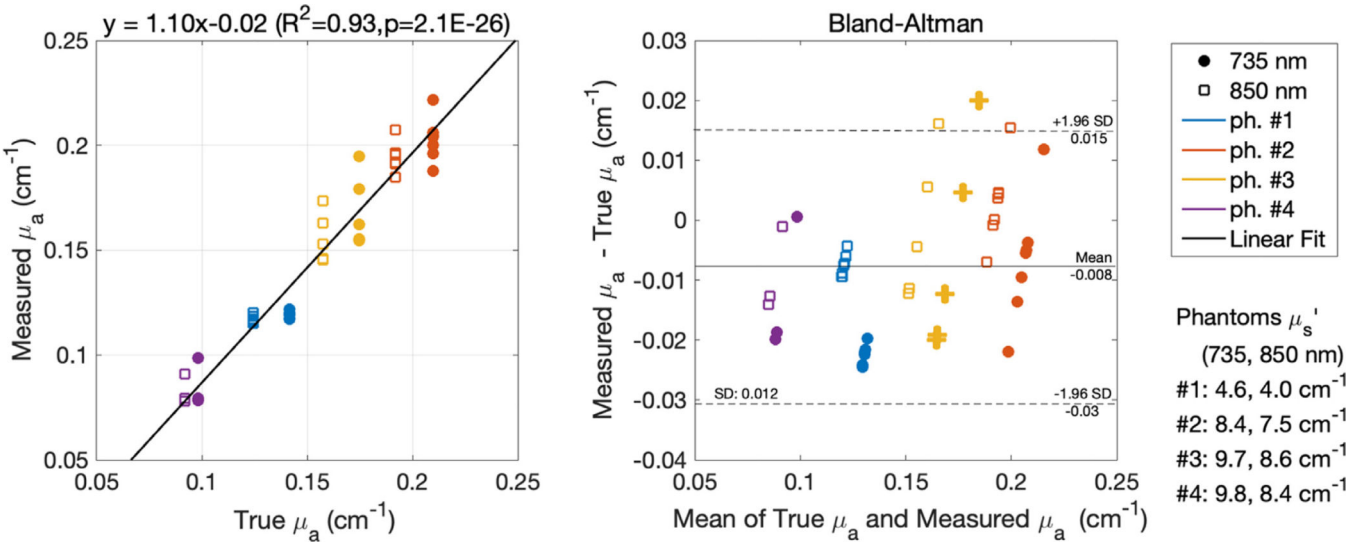

Fig. 6.

Recovering μ_a from tissue-like silicon phantoms: scatterplot of μ_a measured with the FlexNIRS vs. known values and corresponding Bland-Altman plot. For the calculation we used the correct reduced scattering coefficients, not the fixed ones, used in humans.

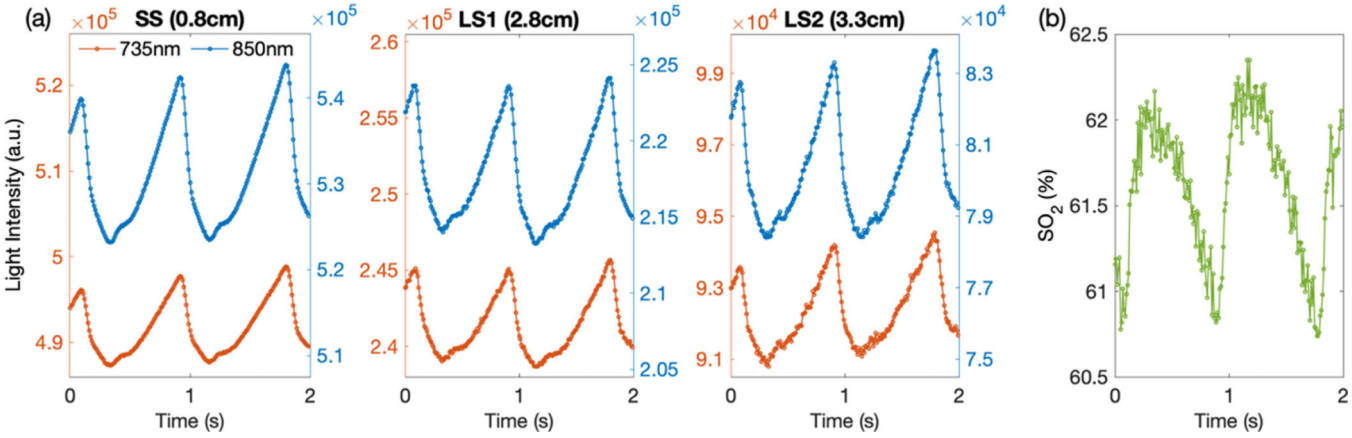

Fig. 7.

(a) A representation of the raw optical signals from a subject's forehead over a 2 s timescale. In each panel, the signals of the two wavelengths were plotted onto two different y-axes with the same scaling factor. Being a plot of the raw light intensity, the pulsation is inverted with diastolic up and systolic down. Signal acquired at 850 nm shows larger amplitude than at 735 nm because of the higher oxy-hemoglobin absorption at this wavelength. (b) Calculated SO_2 with no filters applied, during the same 2 s period. The noise is higher due to the compounding of noise from the 8 intensities used for the calculations.

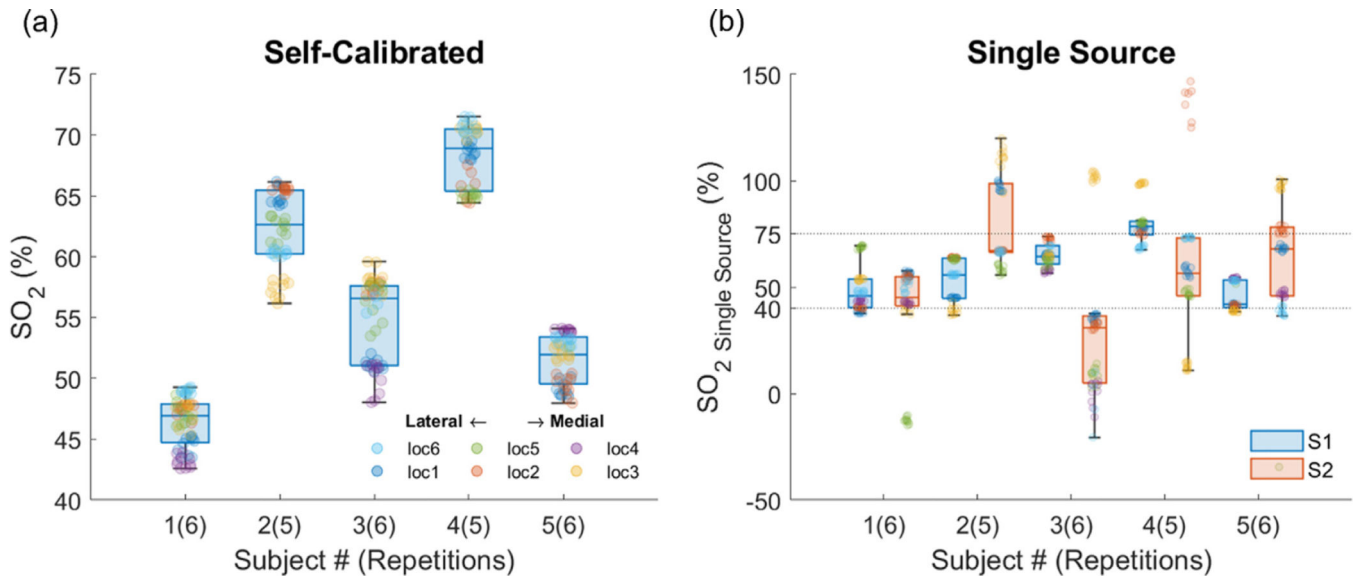

Fig. 8.

Variability of SO_2 across subjects and locations in the forehead. (a) Self-calibrated method, (b) single source results, using S1 (blue bars), and S2 (red bars). Points that do not meet quality criteria are excluded. In the boxplots, the points that deviate more than 1.5 times the interquartile range (Q_3-Q_1) away from Q_1 or Q_3 are considered outliers.

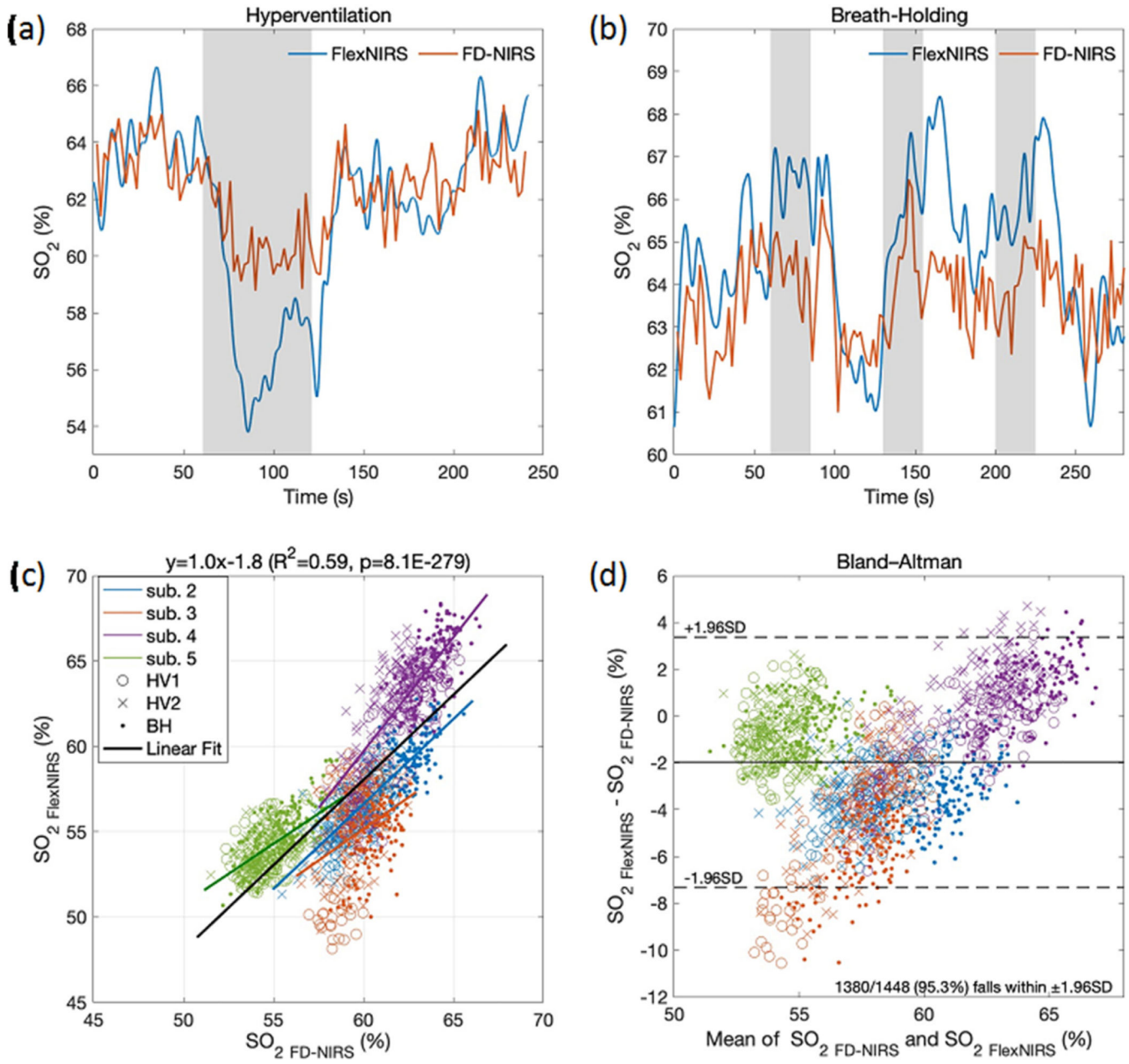

Fig. 9.

(a) and (b) SO_2 time-traces during hyperventilation and breath-holding in a representative subject (subject 4) measured simultaneously with the FlexNIRS (blue) and the FD-NIRS (red) devices. The FlexNIRS data is acquired at 100 Hz and filtered with a low pass filter of 0.5 Hz. The FD-NIRS is acquired at 10 Hz and averaged every 20 points. Gray bars indicate the breathing task period. (c) Scatterplot and (d) Bland-Altman plot of SO_2 measured with the FlexNIRS and the FD-NIRS devices during 2 hyperventilation and 3 breath-holding repetitions. Each point is a 2 s average. For the FlexNIRS, we used fixed reduced scattering coefficients of 6.8 and 5.9 cm^{-1} at 735 and 850 nm, respectively, which differ from the values measured and used for the FD-NIRS SO_2 results. For subjects 2 to 5, the measured

μ_s' are 9.9 and 9.1, 10.3 and 8.2, 10.2 and 8.0, and 13.4 and 11.7 cm^{-1}, at 735 and 850 nm, respectively (average wavelength dependence exponential fit $\left(\mu_s' = 10.7(\lambda/750)^{-1.19}\right)$. Despite the different scattering values, we obtained a good agreement between the two SO_2 measured.

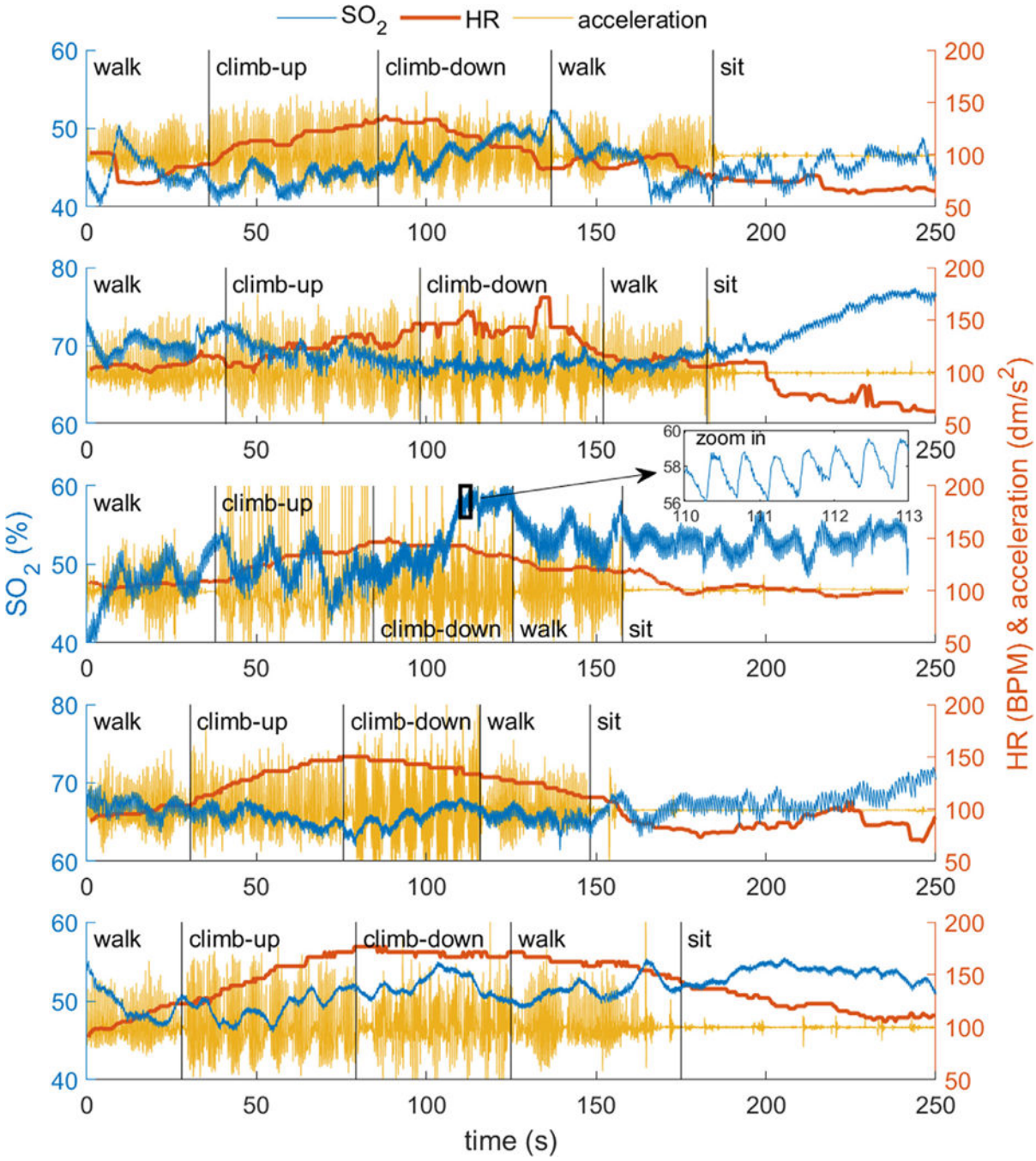

Fig. 10.

SO_2 changes during walking and stair-climbing of the five subjects. Subjects 1 to 5 from top to bottom. In each panel we report SO_2 (blue, left *y*-axis), heart rate (red, right *y*-axis) and acceleration (yellow, right *y*-axis). SO_2 is acquired at 100 Hz with no averaging and the apparent noise in the time traces is arterial pulsation, as shown in the zoomed in panel on subject #3. The average resting heart rate was 98±8 BPM, reached 110 ± 8 BPM during

walking, peaked at 155 ± 15 BPM at the top of the four floors, and returned to 95 ± 22 BPM at the end of the task after resting for 30 s.